



Article

Si₃C Monolayer as an Efficient Metal-Free Catalyst for Nitrate Electrochemical Reduction: A Computational Study

Wanying Guo¹, Tiantian Zhao¹, Fengyu Li^{2,*} , Qinghai Cai¹ and Jingxiang Zhao^{1,*}

- ¹ College of Chemistry and Chemical Engineering, and Key Laboratory of Photonic and Electronic Bandgap Materials, Ministry of Education, Harbin Normal University, Harbin 150025, China; guowanying@stu.hrbnu.edu.cn (W.G.); zhaotiantian@stu.hrbnu.edu.cn (T.Z.); caiqinghai@hrbnu.edu.cn (Q.C.)
- ² School of Physical Science and Technology, Inner Mongolia University, Hohhot 010021, China
- * Correspondence: fengyuli@imu.edu.cn (F.L.); zhaojingxiang@hrbnu.edu.cn (J.Z.)

Abstract: Nitrate electroreduction reaction to ammonia (NO₃ER) holds great promise for both nitrogen pollution removal and valuable ammonia synthesis, which are still dependent on transition-metal-based catalysts at present. However, metal-free catalysts with multiple advantages for such processes have been rarely reported. Herein, by means of density functional theory (DFT) computations, in which the Perdew–Burke–Ernzerhof (PBE) functional is obtained by considering the possible van der Waals (vdW) interaction using the DFT+D3 method, we explored the potential of several two-dimensional (2D) silicon carbide monolayers as metal-free NO₃ER catalysts. Our results revealed that the excellent synergistic effect between the three Si active sites within the Si₃C monolayer enables the sufficient activation of NO₃[−] and promotes its further hydrogenation into NO₂^{*}, NO^{*}, and NH₃, making the Si₃C monolayer exhibit high NO₃ER activity with a low limiting potential of −0.43 V. In particular, such an electrochemical process is highly dependent on the pH value of the electrolytes, in which acidic conditions are more favorable for NO₃ER. Moreover, ab initio molecular dynamics (AIMD) simulations demonstrated the high stability of the Si₃C monolayer. In addition, the Si₃C monolayer shows a low formation energy, excellent electronic properties, a superior suppression effect on competing reactions, and high stability, offering significant advantages for its experimental synthesis and practical applications in electrocatalysis. Thus, a Si₃C monolayer can perform as a promising NO₃ER catalyst, which would open a new avenue to further develop novel metal-free catalysts for NO₃ER.

Keywords: nitrate electroreduction; metal-free catalysts; silicon carbide monolayer; synergistic effect; density functional theory



Citation: Guo, W.; Zhao, T.; Li, F.; Cai, Q.; Zhao, J. Si₃C Monolayer as an Efficient Metal-Free Catalyst for Nitrate Electrochemical Reduction: A Computational Study. *Nanomaterials* **2023**, *13*, 2890. <https://doi.org/10.3390/nano13212890>

Academic Editor: Tomonori Ohba

Received: 4 October 2023

Revised: 26 October 2023

Accepted: 30 October 2023

Published: 31 October 2023



Copyright: © 2023 by the authors. Licensee MDPI, Basel, Switzerland. This article is an open access article distributed under the terms and conditions of the Creative Commons Attribution (CC BY) license (<https://creativecommons.org/licenses/by/4.0/>).

1. Introduction

The ever-increasing discharge of nitrate (NO₃[−])-containing agricultural and industrial sewage causes severe contamination of the soil and water resources, thus posing great threats to global food safety and human health [1,2]. At present, state-of-the-art nitrate treatment of wastewater typically involves the biological and physical strategies of denitrification, which have shown some intrinsic drawbacks [3–5]. For example, biological methods require denitrifying bacteria to convert NO₃[−] into nitrogen, which would be ineffective under extreme conditions, and the biomass materials would need to be post-treated [6]. As for the physical approaches, such as reverse osmosis and ion exchange, they are still focused on displacement rather than elimination, which requires further processing [7]. Chemical reduction is an interesting way to convert NO₃[−] into some desirable products, which can be driven using heat, light, and electrical energy [8]. Among them, the electrochemical reduction of NO₃[−] to ammonia reaction (NO₃ER) has recently emerged as a most promising strategy for water denitrification due to the use of renewable electric energy, mild operation conditions under room temperature and pressure, and without secondary

treatment [9–12]. More importantly, the NH_3 production from this process can serve as a low energy-consuming alternative to the Haber–Bosch process [13–15]. Especially, compared with the nitrogen reduction reaction (NRR), NH_3 synthesized from NO_3^- is more preferable kinetically due to the higher water solubility of NO_3^- and the lower dissociation energy of the N=O bond of NO_3^- than that in a N_2 molecule [16].

However, NO_3^- -to- NH_3 conversion is a very complex process, as it involves the transfer of eight electrons and nine protons, during which NO, NO_2 , N_2O_2 , and N_2 could be produced as undesired byproducts [17–19]. In addition, the competitive hydrogen evolution reaction (HER) renders the NO_3^- ER less selective. Thus, efficient NO_3^- ER catalysts are urgently required. So far, transition-metal-based electrocatalysts, such as alloy [20–22], metal oxide [23,24], and single atom catalysts [25–27], have been extensively investigated and achieved a Faradaic efficiency (FE) higher than 90% for NH_3 synthesis from the NO_3^- ER process. However, the scarcity, high price, and the instability of metal under harsh working conditions greatly hamper its large-scale application and could cause environmental pollution [28]. In this regard, metal-free electrocatalysts exhibit multiple advantages, including their earth abundance, low cost, environment friendliness, long durability, and transformable structures [29,30]. Thus, the development of *metal-free* catalysts for NO_3^- electroreduction into a NH_3 product is of great significance [31,32].

In recent years, various two-dimensional (2D) materials have been widely studied to develop efficient electrocatalysts for some electrochemical reactions due to their unique structure and electronic properties [33–35]. Among them, 2D silicon carbides (Si_xC_y) are of particular interest due to their rich stoichiometries and tunable electronic properties [36]. For example, the SiC , SiC_2 , and SiC_7 monolayers exhibit semiconducting features with band gaps of 2.55 [37], 1.09 [38], and 1.13 eV [39], respectively, and the SiC_3 monolayer is a topological insulator [40]. On the contrary, the Si_3C and SiC_5 monolayers are semi-metal materials [41,42]. These intriguing properties endow 2D Si_xC_y nanomaterials with wide applications in gas sensors [43], Li-ion batteries [44–47], and catalysis [48–53].

With these advantages of 2D Si_xC_y materials in mind, here, we investigated the feasibility of several Si_xC_y materials (including SiC , SiC_2 , SiC_3 , SiC_5 , SiC_7 , and Si_3C monolayers) as catalysts for NO_3^- ER into NH_3 by means of density functional theory (DFT) computations. The results demonstrated that, among these Si_xC_y candidates, the Si_3C monolayer can be identified as the best NO_3^- ER catalyst due to its lowest limiting potential of -0.43 V, which stems from the synergic effect of its three adjacent Si active sites to boost the efficient activation of NO_3^- and the subsequent hydrogenation step. Moreover, the positive charge on Si active sites in the Si_3C monolayer greatly hinders H^+ attacking, guaranteeing its high selectivity toward NO_3^- ER by suppressing the competing HER. In addition, the high stability of the Si_3C monolayer can be verified from a thermal and electrochemical perspective to meet its realistic applications in NO_3^- ER.

2. Computational Methods and Models

All spin-polarized DFT computations were carried out by using a plane-wave basis set, as implemented in the Vienna Ab Initio Simulation Package (VASP 5.4.1) [54,55], in which the projector augmented wave (PAW) potential was adopted for the interactions between electrons and ions [56,57], and the Perdew–Burke–Ernzerhof (PBE) functional [58] within the generalized gradient approximation (GGA) was employed to determine the exchange–correlation interactions with a cutoff energy of 550 eV. The convergence criteria were set to 0.01 eV/Å and 10^{-5} eV, respectively, for the residual force and the energy on each atom during structure formation. The possible van der Waals (vdW) interaction was treated using the empirical correction in Grimme’s method (DFT+D3) [59].

A supercell consisting of $3 \times 3 \times 1$ Si_xC_y unit cells was built with a vacuum space of 20 Å to minimize the interaction between two adjacent images. During the structural relaxation, a $3 \times 3 \times 1$ k -point mesh was employed to sample the 2D Brillouin zone. Ab initio molecular dynamics (AIMD) simulations based on the NVT ensemble [60] were performed to evaluate the thermodynamic stability. To explore the catalytic activity of these Si_xC_y

monolayers for NO₃ER, the computational electrode model (CHE) method [61,62] was employed to compute the free energy diagrams and the corresponding limiting potentials (U_L). Specially, the free energy change (ΔG) of each elementary step can be determined by $\Delta G = \Delta E + \Delta ZPE - T\Delta S + eU$, where ΔE is the reaction energy of the reactant and product species adsorbed on the catalyst, directly obtained from DFT computations, and ΔZPE and ΔS (see Table S1 in Supporting Information) represent the differences in the zero-point energy and entropy of the adsorbed species and the gas phase molecules at 298.15 K, respectively, which can be calculated from the vibrational frequencies. Specially, the entropies of the free molecules (H₂, H₂O, and NH₃) were taken from the NIST database [63], whereas the energy contribution from the configurational entropy in the adsorbed intermediate was neglected. U represents the applied potential, which can be determined as $U = -\Delta G/e$. Thus, U_L corresponds to the applied limiting potential, which can be obtained using the maximum free energy change (ΔG_{max}) to overcome in the NO₃ER process: $U_L = -\Delta G_{max}/e$, well consistent with previous studies [64,65]. To avoid directly computing the energy of NO₃[−], the gaseous HNO₃ was chosen as a reference. The Gibbs adsorption free energy of NO₃[−] (ΔG_{NO₃[−]}) can be computed by $\Delta G_{NO_3^-} = G_{NO_3^-} - G_* - G_{HNO_3(g)} + \frac{1}{2}G_{H_2(g)} + \Delta G_{correct}$, where $G_{NO_3^-}$, G_* , $G_{HNO_3(g)}$, and $G_{H_2(g)}$ represent the Gibbs free energies of the adsorbed NO₃[−], Si_xC_y catalyst, gas-phase HNO₃, and H₂ molecules, respectively, where ΔG_{correct} is the correction for the NO₃[−] adsorption energy, which was set to 0.392 eV based on previous theoretical studies [66–73].

3. Results and Discussion

3.1. Structures and Properties of 2D Si_xC_y Nanomaterials

The optimized structures of these considered 2D Si_xC_y nanomaterials are presented in Figures 1a and S1, while some key parameters are summarized in Table S2. Clearly, all Si_xC_y monolayers have a graphene-like planar structure, which is unlike the puckered structure of silicene. Moreover, the optimized lattice parameters of their unit cells are in the range of 3.09 (SiC) to 7.02 Å (Si₃C), and the lengths of the Si–C bonds range from 1.69 Å (SiC₇) to 1.81 Å (SiC₃ and Si₃C). In particular, within the frameworks of the SiC₂, SiC₃, SiC₅, and SiC₇ monolayers, some C–C bonds can be formed with shortest lengths of about 1.44 Å. However, in the Si₃C monolayer, the Si–Si bonds can be formed with lengths of 2.45 Å. Notably, the above results on the optimized configurations of these Si_xC_y nanomaterials are in good agreement with previous studies [41,45,74] as shown in Table S3, thus ensuring the accuracy of the employed models and methods. Remarkably, the planar configurations of these Si_xC_y monolayers could be related to the ionic-binding features of the Si–C bonds, as shown by the computed charge density distribution in Figures 1b and S1. As expected, due to the larger electronegativity of the C atom than that of the Si atom, there is a significant amount of charge transfer (0.74~2.51 |e[−]|) from the Si atom to the C atom. As a result, the Si atom carries the positive charge, making it exhibit similar electronic properties to the transition metal and thus holding great potential for efficiently activating NO₃[−] in NO₃ER.

To estimate the experimental feasibility of these 2D Si_xC_y materials, we computed their formation energies (E_f) under C-rich and Si-rich conditions according to the following definition: $E_f = (E_{total} - n_C \times \mu_C - n_{Si} \times \mu_{Si}) / (n_C + n_{Si})$, where E_{total} is the total electronic energy of a Si_xC_y monolayer, and n_C and n_{Si} are the number of C and Si atoms in the supercell of the Si_xC_y monolayer according to previous theoretical studies [40]. Moreover, μ_C and μ_{Si} represent the chemical potentials of the C and Si atoms, which greatly depend on the environment conditions. Under C-rich conditions, μ_C was computed from the graphene, and then the chemical potential of the Si atoms was determined by $\mu_{Si} = \mu_{SiC} - \mu_C$, where μ_{SiC} denotes the chemical potential of a SiC unit cell in bulk SiC crystal. On the contrary, the cubic silicon crystal was adopted as the source of Si atoms, and μ_C can be obtained as follows: $\mu_C = \mu_{SiC} - \mu_{Si}$. Based on the above definitions, the computed E_f values of these 2D Si_xC_y systems were summarized in Table S2. Our DFT results showed that the E_f of the SiC monolayer is 0.67 eV, which is independent of the growth conditions due to the same ratio between the Si and C atoms. In contrast, the SiC₂, SiC₃, SiC₅, and

SiC₇ candidates exhibit lower formation energies (0.52~0.66 eV) in C-rich environments than those in Si-rich ones (0.86~1.04 eV), suggesting that such conditions can boost their formation. On the contrary, the Si₃C monolayer prefers to grow in Si-rich conditions due to its smaller E_f value of 0.89 eV. These positive formation energies suggest the synthesis of these Si_xC_y materials still remains challenging in the experiments. Fortunately, rapid progress in the growth of 2D materials on metal-based surfaces by using chemical vapor deposition has been made in recent years [75,76]. For example, Polley et al. reported the synthesis of monolayer honeycomb SiC on ultrathin metal carbide films [77], and Gao et al. synthesized a Si₉C₁₅ monolayer on Ru substrates [78]. In addition, the reaction between graphene and a Si source is another promising synthetic strategy for 2D Si_xC_y materials, such as a quasi-2D SiC₂ monolayer [79].

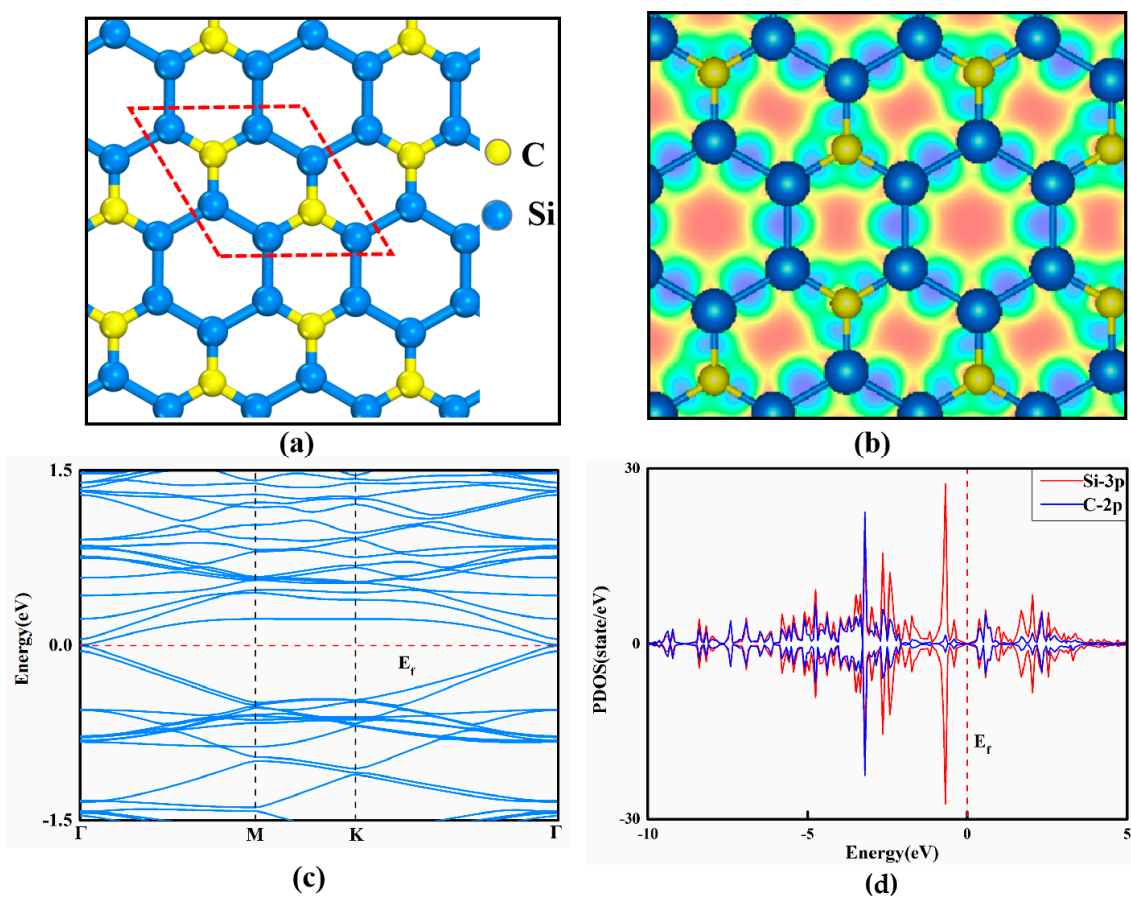


Figure 1. (a) Optimized structure of Si₃C; (b) charge density distribution of Si₃C monolayer (the purple and green areas represent positive and negative charges, respectively); (c) band structure of Si₃C; (d) projected density of states (PDOSs) of Si₃C monolayer. The Fermi level was set to zero for red dotted lines.

The electrical conductivity of a given catalyst has been revealed as an important indicator to evaluate its electrocatalytic activity. In general, excellent electrical conductivity normally facilitates rapid charge transfer for an efficient electrochemical process. Therefore, the band structures of these 2D Si_xC_y candidates were computed to estimate their electrical conductivity. We found that the SiC, SiC₂, or SiC₇ monolayers are semiconductors with large band gaps of 2.55, 0.61, and 0.76 eV (Figure S1), respectively, which would be unfavorable for charge transfer for electrocatalytic reactions. On the contrary, analysis of the band structure shows that SiC₃ (Figure S1) and Si₃C monolayers (Figure 1c) are semi-metallic with the conduction band minimum (CBM) and VBM contacting each other at the point of $\Gamma(k = 0)$ to form a Dirac cone, implying their good electrical conductivity to boost their

applications in electrocatalysis, which mainly originates from the contributions of Si-3p orbitals, as shown by the computed projected density of states (PDOSs, Figure 1d).

3.2. Adsorption and Activation of NO_3^- on Si_xC_y Monolayers

During the process of NO_3^- electroreduction, it is well established that the first step is the adsorption of the nitrate species, which often affects and even determines the whole catalytic reaction pathway. To this end, we next examined the adsorption behavior of the NO_3^- species on these 2D Si_xC_y candidates. To obtain the most stable adsorption structure, three possible initial configurations were taken into account, including 1-O, 2-O, and 3-O patterns, in which the NO_3^- species is adsorbed on the Si or C active sites via its one, two, or three O atoms. After full structural relaxation, the obtained most stable NO_3^- adsorption configurations for these Si_xC_y candidates are shown in Figures 2a and S2, and the computed Gibbs adsorption free energies are summarized in Figure 2b.

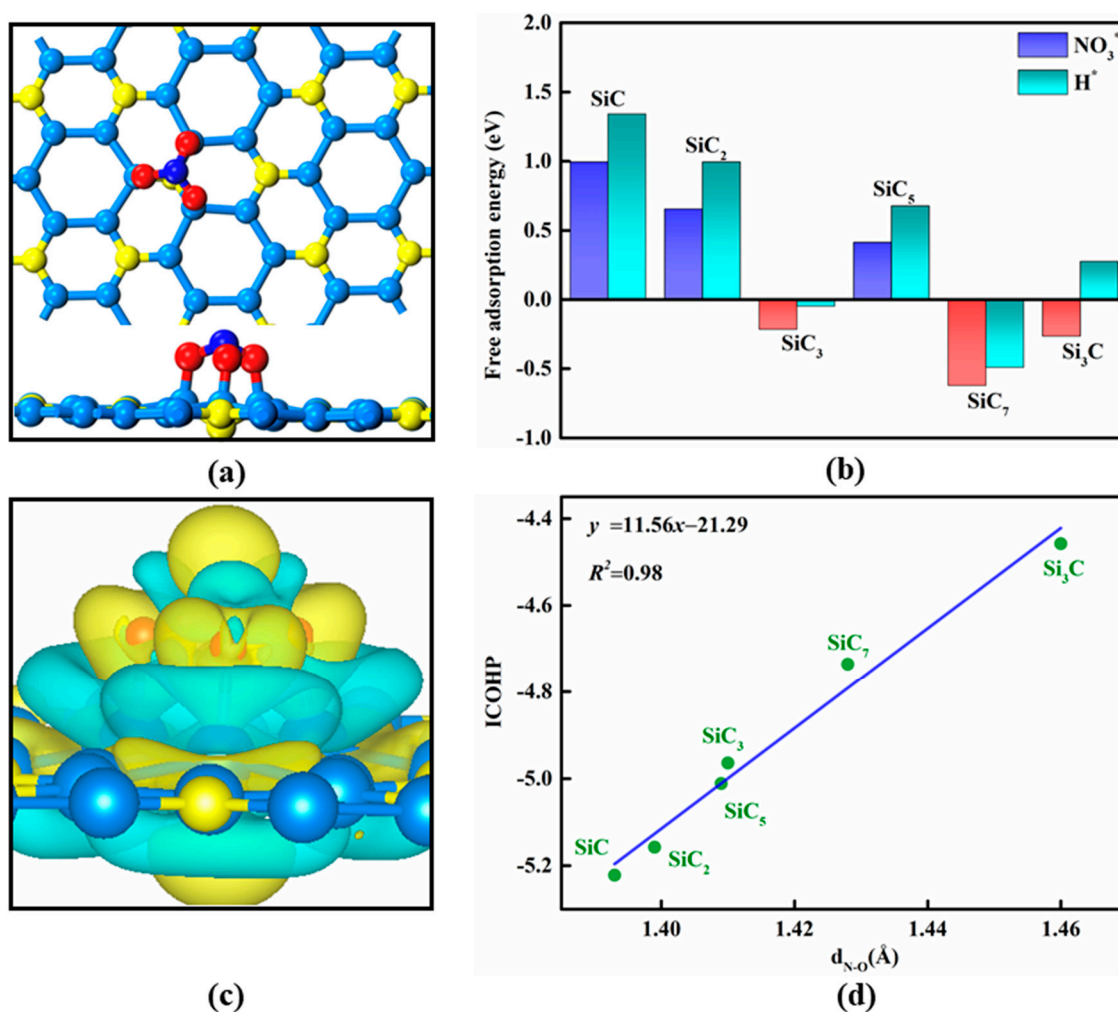


Figure 2. (a) Optimized NO_3^- adsorption structure on Si_3C monolayer; (b) the computed free adsorption energies of NO_3^- and H^+ on Si_xC_y monolayers; (c) charge density differences ($\Delta\rho$) of NO_3^- adsorption on Si_3C monolayer with an isosurface of $0.003 \text{ e } \text{\AA}^{-3}$ (cyan and yellow bubbles denote charge depletion and accumulation, where $\Delta\rho = \rho_{\text{NO}_3^*} - \rho^* - \rho_{\text{NO}_3}$, in which ρ represents the charge density of a given material); (d) the correlation between ICOHP and the distance of N-O bond in the adsorbed NO_3^- ($d_{\text{N-O}}$).

The results showed that NO_3^- is preferable to be adsorbed on SiC , SiC_2 , SiC_3 , SiC_5 , and SiC_7 systems via the 1-O pattern, in which one Si-O bond is formed with a length ranging from 1.74 to 1.79 Å. On a Si_3C monolayer, however, we found that the three O

atoms of NO_3^- species can be adsorbed on three Si sites of this catalyst, forming three Si–O bonds with lengths of 1.74 Å (Figure 2a). Notably, to the best of our knowledge, there is no prior study on such a NO_3^- adsorption configuration via the 3–O pattern, which mainly stems from the unique geometric ensemble effect in the Si_3C monolayer: its three adjacent Si active sites can promote synergistically the sufficient activation of the NO_3^- species.

Based on these aforementioned adsorption configurations, we then evaluated the binding strength of NO_3^- on these 2D Si_xC_y catalysts by computing their corresponding $\Delta G_{\text{NO}_3^*}$ values. Unfortunately, NO_3^- physisorption can be observed on the SiC, SiC₂, and SiC₅ monolayers due to their computed positive $\Delta G_{\text{NO}_3^*}$ values (0.99 eV, 0.65 eV, and 0.41 eV, respectively, Figure 2b), suggesting that NO_3^- cannot be effectively captured by these three Si_xC_y materials, let alone effectively activated. We thus excluded them as promising NO_3ER catalysts from further studies in this work. Conversely, the spontaneous chemisorption of NO_3^- can be achieved on the SiC₃, SiC₇, and Si₃C monolayers with $\Delta G_{\text{NO}_3^*}$ values of −0.21, −0.62, and −0.26 eV, respectively. Moreover, to suppress the unwanted hydrogen evolution reaction (HER) for achieving a high selectivity, the $\Delta G_{\text{NO}_3^*}$ value should be more negative than that of the H^+ species (ΔG_{H^*}), since the H^+ in the electrolytes will block the active sites when H^+ binds too strongly with a given catalyst. Notably, a comparison between ΔG_{H^*} and $\Delta G_{\text{NO}_3^*}$ has been extensively employed to estimate the selectivity of a given catalyst for NO_3ER [65–73]. To this end, the values of $\Delta G_{\text{NO}_3^*}$ and ΔG_{H^*} on the SiC₃, SiC₇, and Si₃C surfaces are presented in Figure 2b for comparison. Clearly, the $\Delta G_{\text{NO}_3^*}$ values are more negative than the corresponding ΔG_{H^*} in the three candidates, especially for the Si₃C monolayer (−0.26 eV for $\Delta G_{\text{NO}_3^*}$ vs. 0.27 eV for ΔG_{H^*}), indicating the good suppressing effect on the undesirable HER and thus ensuring a high selectivity toward the NO_3ER process. Understandably, the positive charges on the Si active sites can greatly hamper H^+ approaching and H^* formation due to the electrostatic repulsion between the positively charged Si sites and H^+ .

To gain a deep insight into the NO_3^- chemisorption, we took the Si₃C monolayer as an example to compute the corresponding charge density differences (Figure 2c). The results show that a considerable amount of negative charge is accumulating between the adsorbed O atoms of the NO_3^* species and Si active sites. According to Bader charge analysis, about 2.30 electrons are transferred from the p-orbitals of the three Si active sites to the empty π^* -orbital of the NO_3^- species, resulting in the sufficient activation of the adsorbed NO_3^- species via the p– π^* interaction, which normally helps trigger the subsequent hydrogenation reaction. In addition, to explain the remarkable difference in the adsorption strength of NO_3^- in these 2D Si_xC_y materials, integrated crystal orbital Hamilton population (ICOHP) analyses of the adsorbed NO_3^* species were computed. Here, a more negative ICOHP value implies a less activated NO_3^* species. As displayed in Figure S3, for the Si₃C monolayer, there is a strong orbital interaction with NO_3^* due to the fully occupied bonding orbitals and nearly unoccupied antibonding orbitals, inducing weaker N=O bonding and more sufficient NO_3^* activation, which can be also confirmed by its less negative ICOHP. Interestingly, a good linear correlation can be observed between the ICOHP and the N–O bond lengths of the adsorbed NO_3^* species (Figure 2d), well accounting for the NO_3^- adsorption trend in these Si_xC_y catalysts, because their different Si active sites determine different bonding/anti-bonding orbital populations.

3.3. Catalytic Performance of SiC₃, SiC₇, and Si₃C Monolayers for NO_3ER

Since sufficient NO_3^- activation has been confirmed on the SiC₃, SiC₇, and Si₃C monolayers, we further evaluated their NO_3ER catalytic performance by computing the free energy changes (ΔG) of all possible elemental steps, which was presented in Figure 3 according to a summary of previous studies on NO_3ER [65–73]. Specially, by computing the ΔG values, we can identify the reaction pathway with the lowest positive free energy change between any two elementary steps, namely, the most favorable reaction pathway.

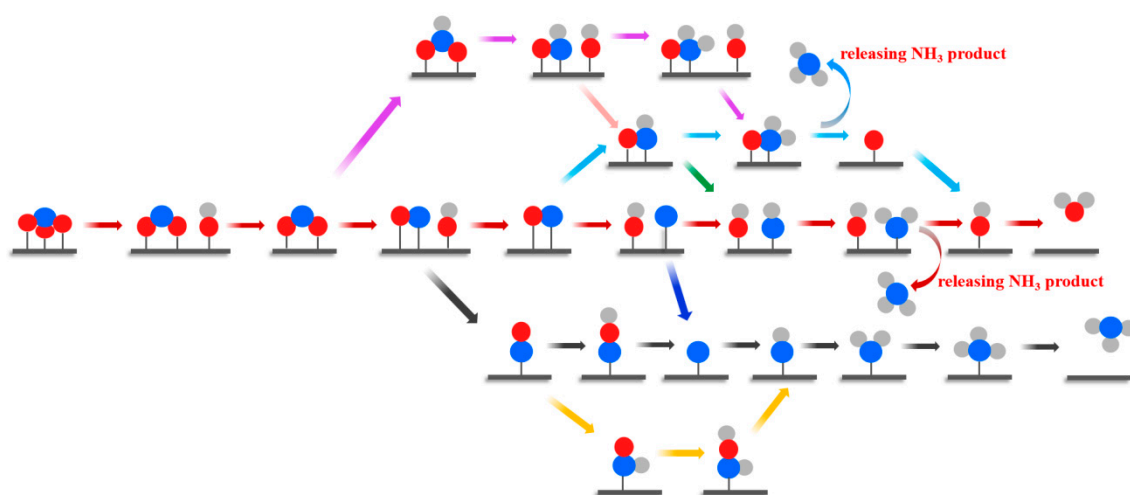


Figure 3. The considered possible reaction pathways for NH_3 synthesis from NO_3ER on Si_3C monolayer.

For simplicity, we again chose the Si_3C monolayer as an example to elaborate the whole NO_3ER process. The obtained most favorable reaction pathway and the involved configurations are shown in Figures 4 and S4, while the computed ΔG values of other possible elementary steps are summarized in Table S4. It can be seen from Figure 4 that NO_3^- can be stably adsorbed on three Si sites by forming three Si–O bonds with a ΔG value of -0.26 eV. Interestingly, the approach of the first ($\text{H}^+ + \text{e}^-$) pair leads to the dissociation of one N–O bond of NO_3^* to generate ($\text{NO}_2^* + \text{OH}^*$) species, which is highly downhill by 1.12 eV in the free energy profile. Kinetically, however, this step of $\text{NO}_3^* \rightarrow \text{NO}_2^* + \text{OH}^*$ requires crossing an energy barrier of 0.95 eV (Figure S5). Subsequently, a H_2O molecule can be released via OH^* hydrogenation, which is slightly endothermic by 0.32 eV. After the formation of H_2O , the remaining NO_2^* , bound to two Si sites with Si–O lengths of 1.79 Å, can react with another ($\text{H}^+ + \text{e}^-$). Due to the synergistic effect of the Si active sites, the hydrogenation of the NO_2^* intermediate also induces the cleavage of one N–O bond spontaneously, forming a ($\text{NO}^* + \text{OH}^*$) group. Remarkably, this step of ($\text{NO}_2^* + \text{H}^+ + \text{e}^- \rightarrow \text{NO}^* + \text{OH}^*$) is highly exothermic by 1.90 eV. Next, an endothermic process for NO^* formation and H_2O desorption is observed with the free energy increased by 0.37 eV. Again, when the H proton attacks the remaining NO^* intermediate, its N–O bond is split into ($\text{N}^* + \text{OH}^*$) with a considerable negative ΔG of -2.54 eV, in which the N atom is adsorbed on the Si–Si bridge site with a length of 1.65 Å. In the subsequent steps, the H proton consecutively attacks the N^* intermediates to generate ($\text{NH}^* + \text{OH}^*$) and ($\text{NH}_2^* + \text{OH}^*$) with ΔG values of -0.62 and -0.07 eV, respectively. Moreover, the NH_2^* species continues to be hydrogenated to achieve a NH_3 product, and this step is slightly exothermic by 0.16 eV. Eventually, the residual OH^* species is reduced to H_2O , and the corresponding energy rises by 0.43 eV.

Overall, the most energetically favorable conversion process from NO_3^- into NH_3 product on the surface of the Si_3C monolayer can be summarized as follows: $\text{NO}_3^- \rightarrow \text{NO}_3^* \rightarrow \text{NO}_2^* + \text{OH}^* \rightarrow \text{NO}_2^* \rightarrow \text{NO}^* + \text{OH}^* \rightarrow \text{NO}^* \rightarrow \text{N}^* + \text{OH}^* \rightarrow \text{NH}^* + \text{OH}^* \rightarrow \text{NH}_2^* + \text{OH}^* \rightarrow \text{OH}^* \rightarrow \text{H}_2\text{O}$ (Figure 4), in which the reduction of OH^* into H_2O can be identified as the potential-determining step (PDS) due to its maximum ΔG value of 0.43 eV. Thus, the U_L of NO_3ER on the Si_3C monolayer is computed to be -0.43 V, which is comparable (even less negative) to some transition metal-based catalysts (-0.34 to -0.53 V) [63–69], suggesting the high NO_3ER catalytic activity of the Si_3C monolayer. In addition to the Si_3C monolayer, we also estimated the activity of the SiC_3 and SiC_7 monolayers for NO_3ER . We found that the NO_3ER process on the two materials is also hampered by OH^* desorption (Figure S6), which requires a high energy input of 0.79 and 1.23 eV, respectively, corresponding to more negative U_L values of -0.79 and -1.23 V than that of Si_3C system (-0.43 V). Of note, to examine the accuracy of the employed PBE function in predicting the catalytic activity, we

re-computed the free energy profile of NO₃ER by using the revised PBE functional (rPBE), in which Si₃C was chosen as an example. Fortunately, we found that the difference in the limiting potential between the two methods is nearly negligible (0.01 V, Figure S7), thus validating the high activity of the Si₃C monolayer toward NO₃ER.

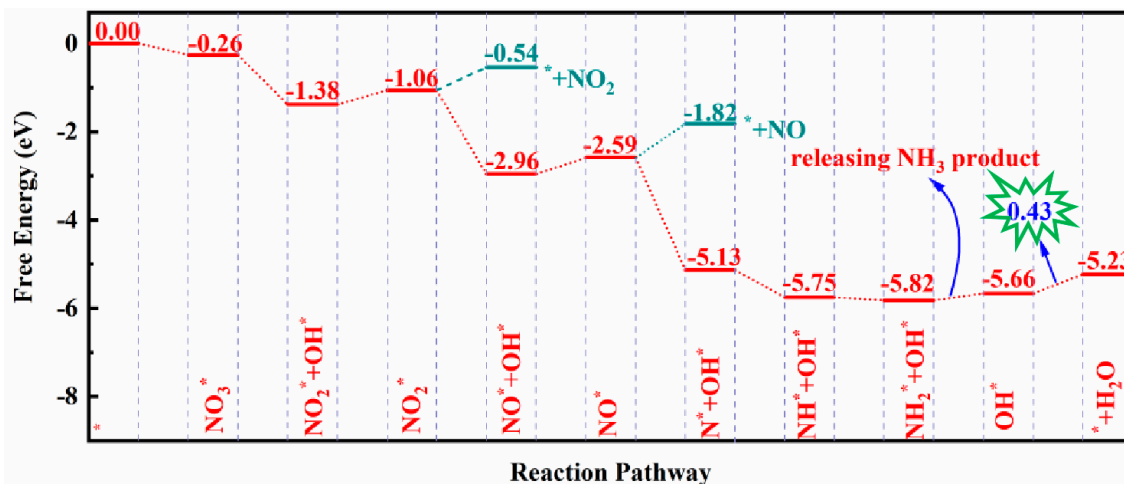


Figure 4. The computed free energy profile for NH₃ synthesis from NO₃ER on Si₃C monolayer.

Another important issue is the selectivity of the Si₃C monolayer toward NO₃ER. We thus examined the reaction pathways to form some N-containing byproducts, including NO₂, NO, and N₂. It can be seen from Figures 4 and S8 that the free energy barriers for the release of NO₂, NO, and N₂ are 0.52, 0.77, and 0.54 eV, respectively, which are much larger than that of NH₃ desorption (0.16 eV). Thus, it is rather difficult to generate these N-based byproducts on the Si₃C monolayer, indicative of its high selectivity toward NH₃ production from NO₃ER. In addition, the HER can be well suppressed due to the weaker H* adsorption on the Si active sites than NO₃⁻ (-0.26 eV for $\Delta G_{\text{NO}_3^*}$ vs. 0.27 eV for ΔG_{H^*}) as in the above discussion (Figure 2b).

3.4. pH-Dependent NO₃ER Activity

It should be noted that NO₃ER generally proceeds in aqueous conditions, which could induce pH-dependent activity in a given electrocatalyst. To examine this concern, the constant potential method (CPM; more computational details can be seen in ESI) developed by Duan et al. [80–84] was employed to explore the pH effects on the NO₃ER catalytic activity on the Si₃C monolayer. The variations of the total electronic energies of the Si₃C monolayer with and without the adsorbed NO₃ER intermediates with the applied electrode potential (standard hydrogen electrode, SHE) are presented in Figure 5a, while the corresponding fitted data are summarized in Table S5, from which a good quadratic relation for all these energy potential points can be observed. Moreover, the adsorption energies (E_{ads} ; more computational details are provided in Supporting Information) of these reaction intermediates at various applied potentials were computed as shown in Figure 5b. As the OH* desorption was identified as the potential-determining step in NO₃ER, its binding strength with the Si₃C monolayer at different pHs and applied potentials is crucial to determine its pH- and potential-dependent activity. The computed E_{ads} values of the OH* species as function pHs and applied potentials are plotted in Figure 5c. The results indicated that alkaline conditions undoubtedly hinder the PDS process due to the stronger OH* adsorption strength on the Si₃C monolayer, suggesting the obvious pH-dependent NO₃ER activity of the Si₃C monolayer. As a result, the Si₃C monolayer always exhibits a higher catalytic activity in acidic solutions (reflected by a lower limiting potential) than that in alkaline ones (Figure 5d). In particular, when the pH is about 2.90, the OH* adsorption is optimal, thus achieving the highest NO₃ER activity with the lowest limiting potential of -0.61 V vs. the reverse hydrogen electrode (RHE) and the involved free

energy profile presented in Figure S9. Noteworthy, highly efficient NO_3ER can be usually achieved in neutral and alkaline media so far. Yet, there are only a few reports on efficient NO_3ER in acidic NO_3^- -containing wastewater [85], which can meet the requirements of industrial processes such as mining, metallurgy, metal processing, and petrochemical and fiber engineering. Especially as compared with neutral/alkaline conditions, NO_3ER in acidic conditions is more beneficial for directly generating fertilizers (such as ammonium sulphate, ammonium chloride, etc.) from a chemical perspective and meanwhile avoiding the volatilization of NH_3 gas from aqueous ammonia in neutral/alkaline products [86,87].

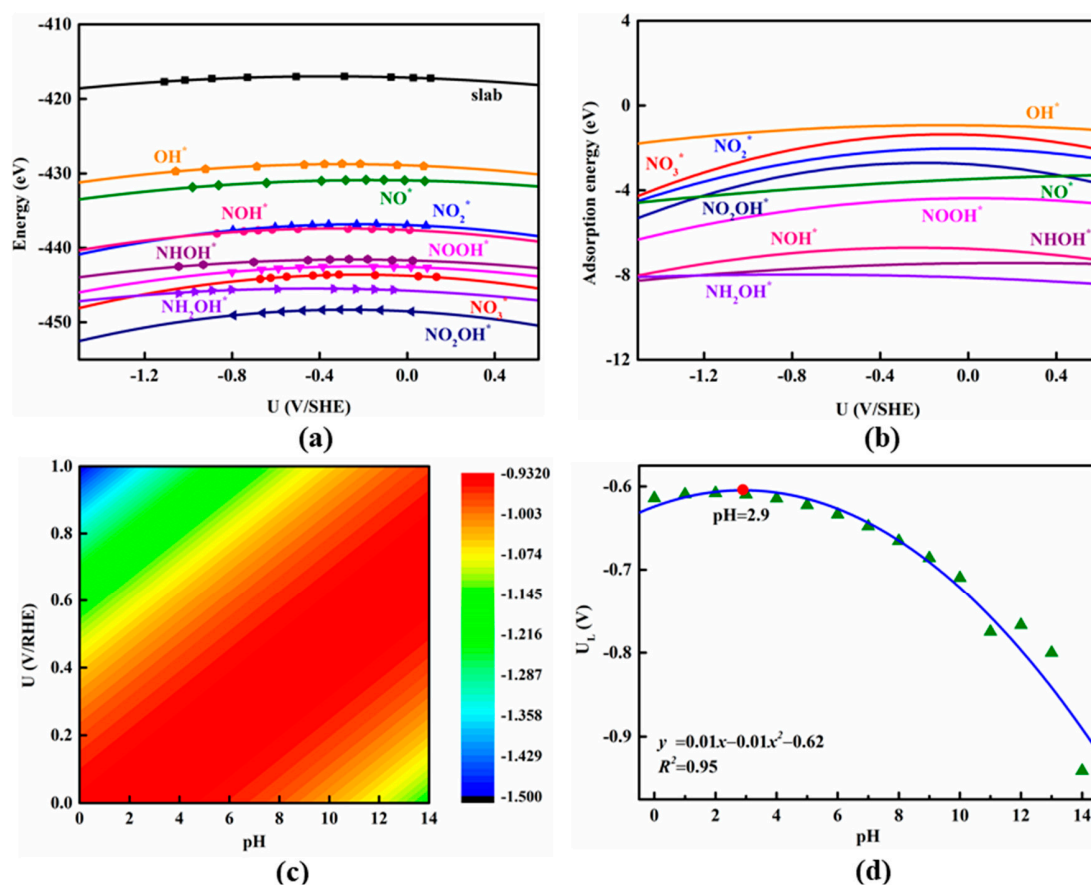


Figure 5. (a) Electronic energies of Si_3C monolayer with and without the adsorbed NO_3ER intermediates as a function of the applied electrode potential; (b) adsorption energies of various NO_3ER intermediates as a function of the applied electrode potential; (c) pH-dependent and potential-dependent contour plot of adsorption energies of OH^* on Si_3C monolayer; (d) the limiting potentials (U_L) of NO_3ER as a function of pH value.

3.5. Stability of Si_3C Monolayer

Stability is a prerequisite for the practical applications of a catalyst. As a result, we evaluated the durability of the Si_3C monolayer by performing ab initio molecular dynamics (AIMD) simulations. The results demonstrated that the geometric structure of the Si_3C monolayer can be well preserved at 500 K after 10 ps (Figure S10a), suggesting its excellent thermal stability. In addition, we also examined the Poisson probability of the bare surfaces of the Si_3C monolayer using the O^*/OH^* species stemming from the aqueous solution under working conditions. Thus, we constructed the surface Pourbaix profile [88–90] of the Si_3C monolayer to examine its surface configurations under different equilibrium potentials and pH values. As shown in Figure S10b, when the electrode potential is 0 V vs. SHE, the basal plane of the Si_3C monolayer is only covered by OH^* species in an alkaline condition. Moreover, the minimum potential required to remove the surface OH^* group on the Si_3C monolayer at pH = 14 (U_R) is -0.39 V, which is less negative than the U_L of

NO₃ER (−0.43 V), indicating the superior electrochemical stability of the Si₃C monolayer against surface oxidation under working conditions.

4. Conclusions

In summary, the potential of several 2D Si_xC_y monolayers as metal-free NO₃ER catalysts for NH₃ synthesis was evaluated by performing comprehensive density functional theory computations. Our results showed that the unique structure of the Si₃C monolayer can sufficiently activate the NO₃[−] reactant by forming a “3–O” adsorption configuration. Moreover, the adsorbed *NO₃ intermediate can be easily hydrogenated into a NH₃ product due to the excellent synergistic effect of the three Si active sites with a low limiting potential of −0.43 V. Meanwhile, the high free energy barriers hinder the formation of NO₂, NO, and N₂ byproducts, and the considerable positive charges on the Si active sites result in weaker H adsorption than NO₃[−], ensuring more favorable NO₃ER than the competitive HER. In addition, the Si₃C monolayer exhibits a low formation energy in Si-rich conditions and good stability, providing great potential for its experimental synthesis and practical application. Remarkably, acidic conditions are beneficial to promote the NO₃[−]-to-NH₃ conversion. The low limiting potential, high selectivity, great promise for synthesis, and high stability render the Si₃C monolayer as a very compelling electrocatalyst for NO₃[−] electrochemical reduction, which may offer new opportunities for efficient nitrate removal and NH₃ synthesis by using metal-free catalysts.

Supplementary Materials: The following supporting information can be downloaded at: <https://www.mdpi.com/article/10.3390/nano13212890/s1>, Figure S1. The optimized structures, charge density distribution, and the band structures of (a) SiC, (b) SiC₂, (c) SiC₃, (d) SiC₅, and (e) SiC₇ monolayers. The isovalue was set to 0.003 e Å^{−3}, and yellow and red bubbles represent positive and negative charges, respectively. The Fermi level was set to zero in red dotted lines; Figure S2. The most stable NO₃^{*} adsorption configurations were viewed from the top and side of these catalysts of (a) SiC, (b) SiC₂, (c) SiC₃, (d) SiC₅, and (e) SiC₇ monolayers; Figure S3. The integrated-crystal orbital Hamilton population (ICOHP) about N–O which from NO₃^{*} is adsorbed species on (a) SiC, (b) SiC₂, (c) SiC₃, (d) SiC₅, (e) SiC₇ and (f) Si₃C monolayers; Figure S4. The involved configurations of intermediates for NO₃ER on Si₃C monolayer; Figure S5. The kinetic process for the dissociation of NO₃^{*} with the help of H⁺ to NO₂^{*} + OH^{*} on Si₃C monolayer; Figure S6. The obtained free energy diagrams of NO₃ER on (a) SiC₃ and (b) SiC₇ catalysts; Figure S7. The free energy diagram of NO₃ER on Si₃C obtained by rPBE method; Figure S8. The obtained free energy diagram of N₂ formation on Si₃C monolayer; Figure S9. The involved free energy profile for NO₃-to-NH₃ electrocatalytic reduction on Si₃C monolayer at pH = 2.90; Figure S10. (a) Variations of temperature and energy as a function of the time for AIMD simulations and (b) Pourbaix profile of Si₃C monolayer; Table S1. The correction of zero-point energy (ZPE, eV) and entropy (TS, eV) of molecules involved in NO₃ER. T is set to 298.15 K; Table S2. The optimized lattice parameters of unit cells (l, Å), lengths of Si–C bonds (d_{Si–C}, Å), C–C bonds (d_{C–C}, Å), and Si–Si bonds (d_{Si–Si}, Å), formation energies under C-rich (E_{f–C}, eV) and Si-rich conditions (E_{Si–C}, eV), the charge transfer (Q, e) from Si atoms to C atoms, and the band gaps (E_{gap}, eV) of 2D Si_xC_y monolayers; Table S3. The data on the optimized structure of Si₃C nanomaterial were compared with those in the literature; Table S4. The all computed free energy changes (ΔG, eV) of each elementary step of Si₃C monolayer. The ΔG values of the selected steps are remarked in red; Table S5. The quadratic relation between the energy (E) of the reaction intermediates and dependence of applied electrochemical potential U.

Author Contributions: Conceptualization, writing—original draft preparation, W.G.; validation, writing—review and editing, formal analysis, T.Z.; data curation, F.L.; writing—review and editing, Q.C.; Supervision, project administration, J.Z. All authors have read and agreed to the published version of the manuscript.

Funding: This work was financially supported in China by the Natural Science Foundation of Heilongjiang Province of China (TD2020B001) and the Natural Science Funds for Distinguished Young Scholars of Heilongjiang Province (No. JC2018004); and the “Grassland Talents” project of Inner Mongolia autonomous region (12000-12102613), and the young science and technology talents cultivation project of Inner Mongolia University (21200-5223708).

Institutional Review Board Statement: Not applicable.

Informed Consent Statement: Not applicable.

Data Availability Statement: The data presented in this study are available on request from the corresponding author.

Conflicts of Interest: The authors declare no competing financial interests.

References

1. Picetti, R.; Deeney, M.; Pastorino, S.; Miller, M.R.; Shah, A.; Leon, D.A.; Dangour, A.D.; Green, R. Nitrate and nitrite contamination in drinking water and cancer risk: A systematic review with meta-analysis. *Environ. Res.* **2022**, *210*, 112988. [[CrossRef](#)]
2. Abascal, E.; Gómez-Coma, L.; Ortiz, I.; Ortiz, A. Global diagnosis of nitrate pollution in groundwater and review of removal technologies. *Sci. Total Environ.* **2022**, *810*, 152233. [[CrossRef](#)]
3. Shrimali, M.; Singh, K.P. New methods of nitrate removal from water. *Environ. Pollut.* **2001**, *112*, 351–359. [[CrossRef](#)]
4. Bhatnagar, A.; Sillanpää, M. A review of emerging adsorbents for nitrate removal from water. *Chem. Eng. J.* **2011**, *168*, 493–504. [[CrossRef](#)]
5. Öztürk, N.; Bektaş, T.E.I. Nitrate removal from aqueous solution by adsorption onto various materials. *J. Hazard. Mater.* **2004**, *112*, 155–162. [[CrossRef](#)]
6. Barrabés, N.; Sá, J. Catalytic nitrate removal from water, past, present and future perspectives. *Appl. Catal. B Environ.* **2011**, *104*, 1–5. [[CrossRef](#)]
7. Liou, Y.H.; Lo, S.L.; Lin, C.J.; Hu, C.Y.; Kuan, W.H.; Weng, S.C. Methods for accelerating nitrate reduction using zerovalent iron at near-neutral pH: effects of H₂-reducing pretreatment and copper deposition. *Environ. Sci. Technol.* **2005**, *39*, 9643–9648. [[CrossRef](#)]
8. Tokazhanov, G.; Ramazanova, E.; Hamid, S.; Bae, S.; Lee, W. Advances in the catalytic reduction of nitrate by metallic catalysts for high efficiency and N₂ selectivity: A review. *Chem. Eng. J.* **2020**, *384*, 123252. [[CrossRef](#)]
9. Xu, H.; Ma, Y.; Chen, J.; Zhang, W.-x.; Yang, J. Electrocatalytic reduction of nitrate—A step towards a sustainable nitrogen cycle. *Chem. Soc. Rev.* **2022**, *51*, 2710–2758. [[CrossRef](#)]
10. Garcia-Segura, S.; Lanzarini-Lopes, M.; Hristovski, K.; Westerhoff, P. Electrocatalytic reduction of nitrate: Fundamentals to full-scale water treatment applications. *Appl. Catal. B Environ.* **2018**, *236*, 546–568. [[CrossRef](#)]
11. Martínez, J.; Ortiz, A.; Ortiz, I. State-of-the-art and perspectives of the catalytic and electrocatalytic reduction of aqueous nitrates. *Appl. Catal. B Environ.* **2017**, *207*, 42–59. [[CrossRef](#)]
12. Meng, S.; Ling, Y.; Yang, M.; Zhao, X.; Osman, A.I.; Al-Muhtaseb, A.a.H.; Rooney, D.W.; Yap, P.-S. Recent research progress of electrocatalytic reduction technology for nitrate wastewater: A review. *J. Environ. Chem. Engin.* **2023**, *11*, 109418. [[CrossRef](#)]
13. Song, W.; Yue, L.; Fan, X.; Luo, Y.; Ying, B.; Sun, S.; Zheng, D.; Liu, Q.; Hamdy, M.S.; Sun, X. Recent progress and strategies on the design of catalysts for electrochemical ammonia synthesis from nitrate reduction. *Inorg. Chem. Front.* **2023**, *10*, 3489–3514. [[CrossRef](#)]
14. Mou, T.; Long, J.; Frauenheim, T.; Xiao, J. Advances in electrochemical ammonia synthesis beyond the use of nitrogen gas as a source. *ChemPlusChem* **2021**, *86*, 1211–1224. [[CrossRef](#)] [[PubMed](#)]
15. Anastasiadou, D.; Van Beek, Y.; Hensen, E.J.M.; Costa Figueiredo, M. Ammonia electrocatalytic synthesis from nitrate. *Electrochem. Sci. Adv.* **2022**, *3*, e2100220. [[CrossRef](#)]
16. Hao, D.; Chen, Z.-g.; Figiela, M.; Stepniak, I.; Wei, W.; Ni, B.-J. Emerging alternative for artificial ammonia synthesis through catalytic nitrate reduction. *J. Mater. Sci. Technol.* **2021**, *77*, 163–168. [[CrossRef](#)]
17. Xiang, T.; Liang, Y.; Zeng, Y.; Deng, J.; Yuan, J.; Xiong, W.; Song, B.; Zhou, C.; Yang, Y. Transition metal single-atom catalysts for the electrocatalytic nitrate reduction: Mechanism, synthesis, characterization, application, and prospects. *Small* **2023**, *19*, 2303732. [[CrossRef](#)]
18. Yang, G.; Zhou, P.; Liang, J.; Li, H.; Wang, F. Opportunities and challenges in aqueous nitrate and nitrite reduction beyond electrocatalysis. *Inorg. Chem. Front.* **2023**, *10*, 4610–4631. [[CrossRef](#)]
19. Liang, X.; Zhu, H.; Yang, X.; Xue, S.; Liang, Z.; Ren, X.; Liu, A.; Wu, G. Recent Advances in designing efficient electrocatalysts for electrochemical nitrate reduction to ammonia. *Small Struct.* **2023**, *4*, 2200202. [[CrossRef](#)]
20. Zhang, G.; Li, X.; Shen, P.; Luo, Y.; Li, X.; Chu, K. PdNi nanosheets boost nitrate electroreduction to ammonia. *J. Environ. Chem. Engin.* **2022**, *10*, 108362. [[CrossRef](#)]
21. Zhang, N.; Zhang, G.; Shen, P.; Zhang, H.; Ma, D.; Chu, K. Lewis acid Fe-V pairs promote nitrate electroreduction to ammonia. *Adv. Funct. Mater.* **2023**, *33*, 2211537. [[CrossRef](#)]
22. Wang, G.; Shen, P.; CenH, K.; Guo, Y.; Zhao, X.; Chu, K. Rare-earth La-doped VS_{2-x} for electrochemical nitrate reduction to ammonia. *Inorg. Chem. Front.* **2023**, *10*, 2014–2021. [[CrossRef](#)]
23. Li, X.; Shen, P.; Li, X.; Ma, D.; Chu, K. Sub-nm RuO_x Clusters on Pd metallene for synergistically enhanced nitrate electroreduction to ammonia. *ACS Nano* **2023**, *17*, 1081–1090. [[CrossRef](#)] [[PubMed](#)]
24. Wang, G.; Shen, P.; Luo, Y.; Li, X.; Li, X.; Chu, K. A vacancy engineered MnO_{2-x} electrocatalyst promotes nitrate electroreduction to ammonia. *Dalton Trans.* **2022**, *51*, 9206–9212. [[CrossRef](#)]

25. Wu, Z.-Y.; Karamad, M.; Yong, X.; Huang, Q.; Cullen, D.A.; Zhu, P.; Xia, C.; Xiao, Q.; Shakouri, M.; Chen, F.-Y.; et al. Electrochemical ammonia synthesis via nitrate reduction on Fe single atom catalyst. *Nat. Commun.* **2021**, *12*, 2870. [[CrossRef](#)]
26. Chen, K.; Ma, Z.; Li, X.; Kang, J.; Ma, D.; Chu, K. Single-atom Bi alloyed Pd metallene for nitrate electroreduction to ammonia. *Adv. Funct. Mater.* **2023**, *33*, 2209890. [[CrossRef](#)]
27. Luo, Y.; Chen, K.; Wang, G.; Zhang, G.; Zhang, N.; Chu, K. Ce-doped MoS_{2-x} nanoflower arrays for electrocatalytic nitrate reduction to ammonia. *Inorg. Chem. Front.* **2023**, *10*, 1543–1551. [[CrossRef](#)]
28. Hu, C.; Lin, Y.; Connell, J.W.; Cheng, H.-M.; Gogotsi, Y.; Titirici, M.-M.; Dai, L. Carbon-based metal-free catalysts for energy storage and environmental remediation. *Adv. Mater.* **2019**, *31*, 1806128. [[CrossRef](#)]
29. Hu, C.; Dai, L. Doping of carbon materials for metal-free electrocatalysis. *Adv. Mater.* **2019**, *31*, 1804672. [[CrossRef](#)]
30. Hu, C.; Paul, R.; Dai, Q.; Dai, L. Carbon-based metal-free electrocatalysts: From oxygen reduction to multifunctional electrocatalysis. *Chem. Soc. Rev.* **2021**, *50*, 11785–11843. [[CrossRef](#)]
31. Li, Y.; Xiao, S.; Li, X.; Chang, C.; Xie, M.; Xu, J.; Yang, Z. A robust metal-free electrocatalyst for nitrate reduction reaction to synthesize ammonia. *Mater. Today Phys.* **2021**, *19*, 100431. [[CrossRef](#)]
32. Villora-Picó, J.J.; Jesús García-Fernández, M.; Sepúlveda-Escribano, A.; Mercedes Pastor-Blas, M. Metal-free abatement of nitrate contaminant from water using a conducting polymer. *Chem. Eng. J.* **2021**, *403*, 126228. [[CrossRef](#)]
33. Chia, X.; Pumera, M. Characteristics and performance of two-dimensional materials for electrocatalysis. *Nat. Catal.* **2018**, *1*, 909–921. [[CrossRef](#)]
34. Li, T.; Jing, T.; Rao, D.; Mourdikoudis, S.; Zuo, Y.; Wang, M. Two-dimensional materials for electrocatalysis and energy storage applications. *Inorg. Chem. Front.* **2022**, *9*, 6008–6046. [[CrossRef](#)]
35. Jin, H.; Guo, C.; Liu, X.; Liu, J.; Vasileff, A.; Jiao, Y.; Zheng, Y.; Qiao, S.-Z. Emerging two-dimensional nanomaterials for electrocatalysis. *Chem. Rev.* **2018**, *118*, 6337–6408. [[CrossRef](#)]
36. Zhou, L.; Dong, H.; Tretiak, S. Recent advances of novel ultrathin two-dimensional silicon carbides from a theoretical perspective. *Nanoscale* **2020**, *12*, 4269–4282. [[CrossRef](#)] [[PubMed](#)]
37. Bekaroglu, E.; Topsakal, M.; Cahangirov, S.; Ciraci, S. First-principles study of defects and adatoms in silicon carbide honeycomb structures. *Phys. Rev. B* **2010**, *81*, 075433. [[CrossRef](#)]
38. Zhou, L.-J.; Zhang, Y.-F.; Wu, L.-M. SiC₂ Siligraphene and Nanotubes: Novel Donor Materials in Excitonic Solar Cells. *Nano Lett.* **2013**, *13*, 5431–5436. [[CrossRef](#)] [[PubMed](#)]
39. Dong, H.; Zhou, L.; Frauenheim, T.; Hou, T.; Lee, S.-T.; Li, Y. SiC₇ siligraphene: A novel donor material with extraordinary sunlight absorption. *Nanoscale* **2016**, *8*, 6994–6999. [[CrossRef](#)] [[PubMed](#)]
40. Zhao, M.; Zhang, R. Two-dimensional topological insulators with binary honeycomb lattices: SiC₃ siligraphene and its analogs. *Phys. Rev. B* **2014**, *89*, 195427. [[CrossRef](#)]
41. Wang, Y.; Li, Y. Ab initio prediction of two-dimensional Si₃C enabling high specific capacity as an anode material for Li/Na/K-ion batteries. *J. Mater. Chem. A* **2020**, *8*, 4274–4282. [[CrossRef](#)]
42. Dong, H.; Wang, L.; Zhou, L.; Hou, T.; Li, Y. Theoretical investigations on novel SiC₅ siligraphene as gas sensor for air pollutants. *Carbon* **2017**, *113*, 114–121. [[CrossRef](#)]
43. Farmanzadeh, D.; Ardehijani, N.A. Adsorption of O₃, SO₂ and NO₂ molecules on the surface of pure and Fe-doped silicon carbide nanosheets: A computational study. *Appl. Surf. Sci.* **2018**, *462*, 685–692. [[CrossRef](#)]
44. Wang, H.; Wu, M.; Lei, X.; Tian, Z.; Xu, B.; Huang, K.; Ouyang, C. Siligraphene as a promising anode material for lithium-ion batteries predicted from first-principles calculations. *Nano Energy* **2018**, *49*, 67–76. [[CrossRef](#)]
45. Hu, Y.; Liu, Y.; Huang, Y.; Lin, H. Flexible Si₃C monolayer: A superior anode for high-performance non-lithium ion batteries. *Colloids Surf. A Physicochem. Eng. Asp.* **2022**, *637*, 128238. [[CrossRef](#)]
46. Dong, Y.; Wei, W.; Lv, X.; Huang, B.; Dai, Y. Semimetallic Si₃C as a high capacity anode material for advanced lithium ion batteries. *Appl. Surf. Sci.* **2019**, *479*, 519–524. [[CrossRef](#)]
47. Zhao, Y.; Zhao, J.; Cai, Q. SiC₂ siligraphene as a promising anchoring material for lithium-sulfur batteries: A computational study. *Appl. Surf. Sci.* **2018**, *440*, 889–896. [[CrossRef](#)]
48. Sinthika, S.; Vala, S.T.; Kawazoe, Y.; Thapa, R. CO oxidation prefers the Eley–Rideal or Langmuir–Hinshelwood pathway: Monolayer vs thin film of SiC. *ACS Appl. Mater. Interfaces* **2016**, *8*, 5290–5299. [[CrossRef](#)]
49. Guo, Z.; Qiu, S.; Li, H.; Xu, Y.; Langford, S.J.; Sun, C. Electrocatalytic dinitrogen reduction reaction on silicon carbide: A density functional theory study. *Phys. Chem. Chem. Phys.* **2020**, *22*, 21761–21767. [[CrossRef](#)]
50. Guo, Z.; Jasin Arachchige, L.; Qiu, S.; Zhang, X.; Xu, Y.; Langford, S.J.; Sun, C. p-block element-doped silicon nanowires for nitrogen reduction reaction: A DFT study. *Nanoscale* **2021**, *13*, 14935–14944. [[CrossRef](#)]
51. Guo, Z.; Wang, T.; Liu, H.; Qiu, S.; Zhang, X.; Xu, Y.; Langford, S.J.; Sun, C. Defective 2D silicon phosphide monolayers for the nitrogen reduction reaction: A DFT study. *Nanoscale* **2022**, *14*, 5782–5793. [[CrossRef](#)] [[PubMed](#)]
52. Liu, C.; Zheng, H.; Wang, T.; Zhang, X.; Guo, Z.; Li, H. Efficient asymmetrical silicon–metal dimer electrocatalysts for the nitrogen reduction reaction. *Phys. Chem. Chem. Phys.* **2023**, *25*, 13126–13135. [[CrossRef](#)] [[PubMed](#)]
53. Zheng, M.; Li, Y.; Ding, K.; Zhang, Y.; Chen, W.; Lin, W. Nitrogen fixation on metal-free SiC(111) polar surfaces. *J. Mater. Chem. A* **2020**, *8*, 7412–7421. [[CrossRef](#)]
54. Kresse, G.; Hafner, J. Ab-initio molecular-dynamics for liquid-metals. *Phys. Rev. B* **1993**, *47*, 558–561. [[CrossRef](#)]

55. Kresse, G.; Furthmüller, J. Efficient iterative schemes for ab initio total-energy calculations using a plane-wave basis set. *Phys. Rev. B* **1996**, *54*, 11169–11186. [[CrossRef](#)]
56. Blochl, P.E. Projector augmented-wave method. *Phys. Rev. B* **1994**, *50*, 17953–17979. [[CrossRef](#)]
57. Kresse, G.; Joubert, D. From ultrasoft pseudopotentials to the projector augmented-wave method. *Phys. Rev. B* **1999**, *59*, 1758–1775. [[CrossRef](#)]
58. Perdew, J.P.; Burke, K.; Ernzerhof, M. Generalized gradient approximation made simple. *Phys. Rev. Lett.* **1996**, *77*, 3865–3868. [[CrossRef](#)]
59. Grimme, S. Semiempirical GGA-type density functional constructed with a long-range dispersion correction. *J. Comput. Chem.* **2006**, *27*, 1787–1799. [[CrossRef](#)]
60. Martyna, G.J.; Klein, M.L.; Tuckerman, M. Nose-Hoover chains—the canonical ensemble via continuous dynamics. *J. Chem. Phys.* **1992**, *97*, 2635–2643. [[CrossRef](#)]
61. Nørskov, J.K.; Rossmeisl, J.; Logadottir, A.; Lindqvist, L.; Kitchin, J.R.; Bligaard, T.; Jonsson, H. Origin of the overpotential for oxygen reduction at a fuel-cell cathode. *J. Phys. Chem. B* **2004**, *108*, 17886–17892. [[CrossRef](#)]
62. Peterson, A.A.; Abild-Pedersen, F.; Studt, F.; Rossmeisl, J.; Nørskov, J.K. How copper catalyzes the electroreduction of carbon dioxide into hydrocarbon fuels. *Energy Environ. Sci.* **2010**, *3*, 1311–1315. [[CrossRef](#)]
63. Johnson, R. *Computational Chemistry Comparison and Benchmark Database, NIST Standard Reference Database 101*; National Institute of Standards and Technology: Gaithersburg, MD, USA, 2002.
64. Sun, Y.; Shi, W.; Sun, M.; Fang, Q.; Ren, X.; Yan, Y.; Gan, Z.; Fu, Y.; Elmarakbi, A.; Li, Z.; et al. Molybdenum based 2D conductive Metal–Organic frameworks as efficient single-atom electrocatalysts for N₂ reduction: A density functional theory study. *Int. J. Hydrog. Energy* **2023**, *48*, 19972–19983. [[CrossRef](#)]
65. Dai, T.; Wang, Z.; Wen, Z.; Lang, X.; Jiang, Q. Tailoring Electronic Structure of Copper Twin Boundaries Toward Highly Efficient Nitrogen Reduction Reaction. *ChemSusChem* **2022**, *15*, e202201189. [[CrossRef](#)] [[PubMed](#)]
66. Sathishkumar, N.; Chen, H.-T. Mechanistic understanding of the electrocatalytic nitrate reduction activity of double-atom catalysts. *J. Phys. Chem. C* **2023**, *127*, 994–1005. [[CrossRef](#)]
67. Niu, H.; Zhang, Z.; Wang, X.; Wan, X.; Shao, C.; Guo, Y. Theoretical insights into the mechanism of selective nitrate-to-ammonia electroreduction on single-atom catalysts. *Adv. Funct. Mater.* **2021**, *31*, 2008533. [[CrossRef](#)]
68. Rehman, F.; Kwon, S.; Musgrave, C.B.; Tamtaji, M.; Goddard, W.A.; Luo, Z. High-throughput screening to predict highly active dual-atom catalysts for electrocatalytic reduction of nitrate to ammonia. *Nano Energy* **2022**, *103*, 107866. [[CrossRef](#)]
69. Wu, D.; Lv, P.; Wu, J.; He, B.; Li, X.; Chu, K.; Jia, Y.; Ma, D. Catalytic active centers beyond transition metals: Atomically dispersed alkaline-earth metals for the electroreduction of nitrate to ammonia. *J. Mater. Chem. A* **2023**, *11*, 1817–1828. [[CrossRef](#)]
70. Sathishkumar, N.; Wu, S.-Y.; Chen, H.-T. Mechanistic exploring the catalytic activity of single-atom catalysts anchored in graphitic carbon nitride toward electroreduction of nitrate-to-ammonia. *Appl. Surf. Sci.* **2022**, *598*, 153829. [[CrossRef](#)]
71. Wu, J.; Li, J.-H.; Yu, Y.-X. Theoretical exploration of electrochemical nitrate reduction reaction activities on transition-metal-doped h-BP. *J. Phys. Chem. Lett.* **2021**, *12*, 3968–3975. [[CrossRef](#)]
72. Wang, Y.; Wu, D.; Lv, P.; He, B.; Li, X.; Ma, D.; Jia, Y. Theoretical insights into the electroreduction of nitrate to ammonia on graphene-based single-atom catalysts. *Nanoscale* **2022**, *14*, 10862–10872. [[CrossRef](#)] [[PubMed](#)]
73. Wang, Y.; Shao, M. Theoretical screening of transition metal–N₄-doped graphene for electroreduction of nitrate. *ACS Catal.* **2022**, *12*, 5407–5415. [[CrossRef](#)]
74. Yin, N.; Dai, Y.; Wei, W.; Huang, B. Electronic structure engineering in silicene via atom substitution and a new two-dimensional Dirac structure Si₃C. *Phys. E Low-Dimens. Syst. Nanostruct.* **2018**, *98*, 39–44. [[CrossRef](#)]
75. Jiang, J.; Li, N.; Zou, J.; Zhou, X.; Eda, G.; Zhang, Q.; Zhang, H.; Li, L.-J.; Zhai, T.; Wee, A.T.S. Synergistic additive-mediated CVD growth and chemical modification of 2D materials. *Chem. Soc. Rev.* **2019**, *48*, 4639–4654. [[CrossRef](#)]
76. Ji, Q.; Zhang, Y.; Zhang, Y.; Liu, Z. Chemical vapour deposition of group-VIB metal dichalcogenide monolayers: Engineered substrates from amorphous to single crystalline. *Chem. Soc. Rev.* **2015**, *44*, 2587–2602. [[CrossRef](#)]
77. Polley, C.M.; Fedderwitz, H.; Balasubramanian, T.; Zakharov, A.A.; Yakimova, R.; Bäcke, O.; Ekman, J.; Dash, S.P.; Kubatkin, S.; Lara-Avila, S. Bottom-Up Growth of Monolayer Honeycomb SiC. *Phys. Rev. Lett.* **2023**, *130*, 076203. [[CrossRef](#)]
78. Gao, Z.-Y.; Xu, W.; Gao, Y.; Guzman, R.; Guo, H.; Wang, X.; Zheng, Q.; Zhu, Z.; Zhang, Y.-Y.; Lin, X.; et al. Experimental Realization of Atomic Monolayer Si₉C₁₅. *Adv. Mater.* **2022**, *34*, 2204779. [[CrossRef](#)]
79. Lin, S.; Zhang, S.; Li, X.; Xu, W.; Pi, X.; Liu, X.; Wang, F.; Wu, H.; Chen, H. Quasi-two-dimensional SiC and SiC₂: Interaction of silicon and carbon at atomic thin lattice plane. *J. Phys. Chem. C* **2015**, *119*, 19772–19779. [[CrossRef](#)]
80. Duan, Z.; Henkelman, G. Theoretical resolution of the exceptional oxygen reduction activity of Au(100) in alkaline media. *ACS Catal.* **2019**, *9*, 5567–5573. [[CrossRef](#)]
81. Duan, Z.; Henkelman, G. Surface charge and electrostatic spin crossover effects in CoN₄ electrocatalysts. *ACS Catal.* **2020**, *10*, 12148–12155. [[CrossRef](#)]
82. Liu, W.; Duan, Z.; Wang, W. Water oxidation-induced surface reconstruction and dissolution at the RuO₂ (110) surface revealed by first-principles simulation. *J. Phys. Chem. C* **2023**, *127*, 5334–5342. [[CrossRef](#)]
83. Duan, Z.; Henkelman, G. Identification of active sites of pure and nitrogen-doped carbon materials for oxygen reduction reaction using constant-potential calculations. *J. Phys. Chem. C* **2020**, *124*, 12016–12023. [[CrossRef](#)]

84. Zheng, T.; Wang, J.; Xia, Z.; Wang, G.; Duan, Z. Spin-dependent active centers in Fe–N–C oxygen reduction catalysts revealed by constant-potential density functional theory. *J. Mater. Chem. A* **2023**, *11*, 19360–19373. [[CrossRef](#)]
85. Lv, Y.; Ke, S.-W.; Gu, Y.; Tian, B.; Tang, L.; Ran, P.; Zhao, Y.; Ma, J.; Zou, J.-L.; Ding, M. Highly efficient electrochemical nitrate reduction to ammonia in strong acid conditions with Fe₂M-trinuclear-cluster metal-organic frameworks. *Angew. Chem. Int. Ed.* **2023**, *62*, e202305246. [[CrossRef](#)] [[PubMed](#)]
86. Chen, F.-Y.; Wu, Z.-Y.; Gupta, S.; River, D.J.; Lambetts, S.V.; Pecaut, S.; King, J.Y.T.; Zhu, P.; Finfrock, Y.Z.; Meria, D.M.; et al. Efficient conversion of low-concentration nitrate sources into ammonia on a Ru-dispersed Cu nanowire electrocatalyst. *Nat. Nanotechnol.* **2022**, *17*, 759–767. [[CrossRef](#)]
87. Yang, J.; Gao, H.; Hu, G.; Wang, S.; Zhang, Y. Novel process of removal of sulfur dioxide by aqueous Ammonia–fulvic acid solution with ammonia escape inhibition. *Energy Fuels* **2016**, *30*, 3205–3218. [[CrossRef](#)]
88. Zhu, X.; Zhou, X.; Jing, Y.; Li, Y. Electrochemical synthesis of urea on MBenes. *Nat. Commun.* **2021**, *12*, 4080. [[CrossRef](#)]
89. Jiao, D.; Wang, Z.; Liu, Y.; Cai, Q.; Zhao, J.; Cabrera, C.R.; Chen, Z. Mo₂P monolayer as a superior electrocatalyst for urea synthesis from nitrogen and carbon dioxide fixation: A computational study. *Energy Environ. Mater.* **2022**. [[CrossRef](#)]
90. Sun, Y.; Wang, Z.; Liu, Y.; Cai, Q.; Zhao, J. The β-PdBi₂ monolayer for efficient electrocatalytic NO reduction to NH₃: A computational study. *Inorg. Chem. Front.* **2023**, *10*, 2677–2688. [[CrossRef](#)]

Disclaimer/Publisher’s Note: The statements, opinions and data contained in all publications are solely those of the individual author(s) and contributor(s) and not of MDPI and/or the editor(s). MDPI and/or the editor(s) disclaim responsibility for any injury to people or property resulting from any ideas, methods, instructions or products referred to in the content.